Copper Loss Analysis of a Multi-winding High-frequency Transformer for a Magnetically-coupled Residential Micro-grid

Mohammad Jafari, *Member, IEEE,* Zahra Malekjamshidi, *Student Member, IEEE,* and Jianguo Zhu, *Senior Member, IEEE*

***Abstract*— Improvements in characteristics of magnetic materials and switching devices have provided the feasibility of replacing the electrical buses with high-frequency magnetic links in small-scale micro-grids. This can effectively reduce the number of voltage conversion stages, size and cost of the micro-grid, and isolate the sources and loads. To optimally design the magnetic link, an accurate evaluation of copper loss of the windings considering both the current waveforms and parasitic effects are required. This paper studies the copper loss analysis of a three-winding high-frequency magnetic link for residential micro-grid applications. Due to the non-sinusoidal nature of the voltages and currents, the loss analysis is carried out on a harmonic basis taking into account the variations of phase shift, duty ratio and amplitude of the waveforms. The high-frequency parasitic phenomena including the skin and proximity effects are taken into account. The maximum and minimum copper loss operating conditions of the magnetic link and their dependency on the phase shift angle and the duty ratio of the connected waveforms are studied. A prototype of the micro-grid including the magnetic link is developed to validate the theoretical analysis, evaluate the micro-grid efficiency and perform the loss breakdown.**

***Index Terms*—Copper loss, high-frequency, magnetic link, phase-shift converter, proximity, skin effects**

I. Introduction

HIGH-FREQUENCY magnetic links have attracted a lot of research interests for their application in grid integration of renewable energy resources. The magnetic link is a multi-winding high-frequency transformer which provides bidirectional paths for magnetic fluxes and power flows between different ports. As a feasible replacement for conventional electrical buses, it can be used to integrate renewable energies in smart grids [1]-[3]. It can reduce effectively the number of conversion stages and improve the conversion efficiency using lossless switching devices and modern soft magnetic materials [4]-[6]. Other advantages are galvanic isolation and bidirectional power flow capability between different converter ports [6]-[8]. Fig.1 illustrates two renewable energy systems with and without the magnetic link. The dashed lines show that the power flow path from PV array to the battery has been reduced effectively with the use of the magnetic link. Therefore, employing the magnetic link can reduce the number of voltage conversion units, increase the system efficiency and reduce the system's size and cost. Another application of the magnetic link is in the conversion cells of the solid-state transformers (SSTs') as presented in Fig.2 [9]. It can be seen that the magnetic link can be used as an interface in the dc-dc converter stage to reduce the number of conversion cells. To optimally design the magnetic link, the winding loss should be accurately evaluated considering the non-sinusoidal effects of voltage and current waveforms [10]-[11]. This particularly is important in the case of SST application due to the modular structure and impact of the magnetic link on the system's efficiency [12].

Due to the skin and proximity effects caused by the high-frequency time-varying harmonics of non-sinusoidal currents, the current distribution in the wire cross section is non-uniform [13]-[19]. Taking into account the dependency of these effects on the operating frequency, a frequency-dependent resistance model was used to analyze the copper loss [14]-[18].To reduce the copper loss, Litz wires are recommended for high-frequency applications [14]-[19]. The loss evaluation of Litz wire windings is mainly based on either numerical [14], [15] or analytical [16]–[24] field analysis. The numerical methods can provide more accurate results although they are relatively complicated and computationally expensive. On the contrary, the analytical methods are simple for design purposes and can present reasonably good accuracy where Litz wire strand radius remains below the skin depth [10], [25]. The analytical methods, in turn, can be divided into three groups [10]. A majority of works are based on Dowell's work in 1966 on loss analysis of foil and round conductors using the Maxwell's equations in the Cartesian coordinate [16]. The Dowell's method for foil conductors was extended to the Litz wire windings of the same cross-section area and a porosity factor has been applied to the resultant equation to increase the accuracy [17]-[18]. The second approach known as the Ferreira method is based on the exact field solution of a

Manuscript received January 22, 2018; revised April 28, 2018 and June 7, 2018; accepted July 16, 2018.

M. Jafari, and Z. Malekjamshidi are with the School of Electrical and Data Engineering, University of Technology Sydney, Sydney, NSW,2007, Australia, (e-mail: mohammad.jafari@uts.edu.au; zahra.malekjamshidi@uts.edu.au).

J. Zhu is with the School of Electrical and Information Engineering, The University of Sydney, Sydney, NSW 2006, Australia. (e-mail:, Jianguo.zhu@sydney.edu.au).

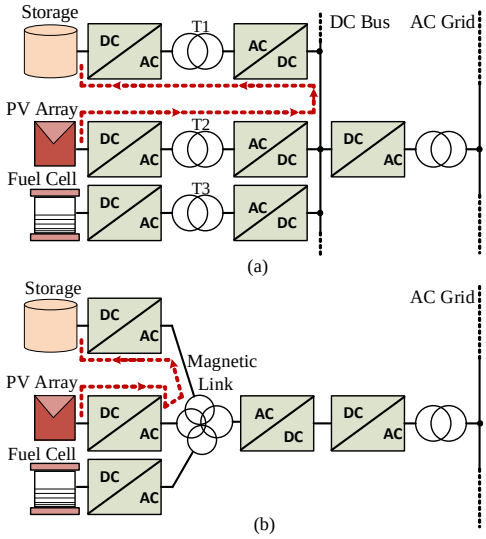

Fig.1. Comparing two micro-grids, (a) without, and (b) with the magnetic link

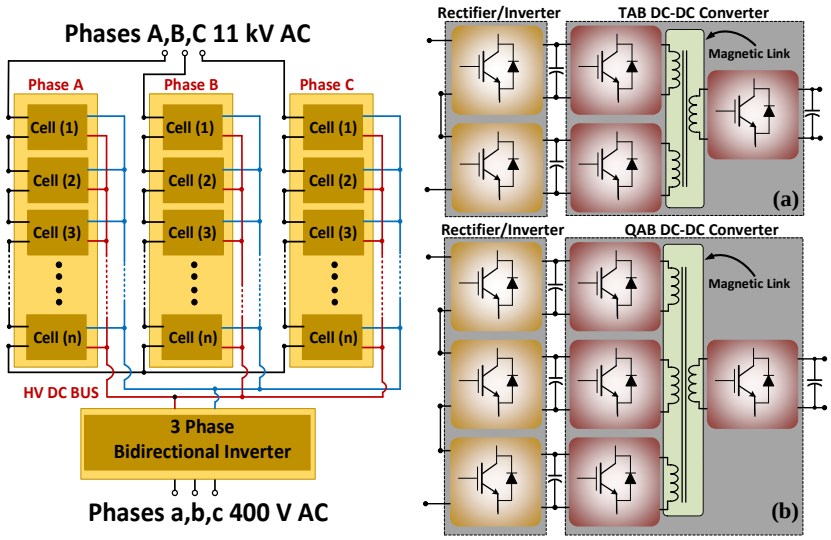

Fig.2. Application of the magnetic link in the (a) TAB or (b) QAB dc-dc conversion cells as a part of a solid state transformer

stand-alone round conductor using the Bessel functions [19]. The analysis was later extended to a complete winding [20], [21] and an expression was introduced using modified Bessel functions to improve the accuracy of method in high-frequency applications [22]. In the third group, the conduction loss is calculated by using the complex conductor permeability [23]. The method provides a good accuracy although it is complicated to determine the real and imaginary parts of the winding permeability [10]. The first two methods are widely used in the literature and their accuracy is compared in [21] and [24]. Both methods can provide good accuracy, especially where strand diameter is much smaller than the skin depth [10], [18], [21].

A detailed study on copper loss analysis of buck and flyback dc-dc converters under variable duty ratio based on the first analytical method is presented recently [26]-[28] although none of these studies deal with the multiple winding transformer supplied by the square wave voltages with simultaneous variation in the phase shift, amplitude and duty ratio. This can be applied to the multi-port phase shift converters with bidirectional power flow due to their recent applications in the solid state transformers (SSTs) and integration of renewable energy systems [9],[29].

In this paper, a general method of copper loss calculation in the multi-winding magnetic links supplied by the variable phase shift, amplitude, and the duty ratio square-wave voltages is proposed [30]. The method can be applied to the multi-winding magnetic links with the square-window magnetic cores for energy integration in micro-grids or SST applications. In this paper, it is particularly used for a residential micro-grid application as it provides more flexibility for study due to the asymmetrical operation of the converter ports. The maximum and minimum loss conditions are defined for two common micro-grid operation modes known as dual active bridge (DAB) and triple active bridge (TAB). To validate the analytical method, a prototype of the magnetic link has been designed and developed. The copper loss of all windings is measured experimentally and compared to the analytical calculations. The resultant loss is further used to perform the loss breakdown of the converter for both DAB and TAB operation modes and obtain the efficiency profiles. To measure the winding resistance and leakage inductance of the windings as a function of frequency, a set of harmonic-based differentially and cumulatively series-coupling tests under the nominal voltage and current is conducted.

II. Structure of the Proposed Residential Micro-grid

The proposed micro-grid topology including a three-winding magnetic link is illustrated in Fig.3 and experimentally developed as presented in Fig.4. As can be seen, the proposed topology includes four ports. Port one, two and three are linked together through the magnetic link, forming a TAB phase shift converter. They are used to convert the dc voltage of fuel cell, PV and inverter bus to a high-frequency ac voltage fed to the windings of the magnetic link. Port four links the battery to the fuel cell bus to store the surplus energy of the system and release it when is required. It also operates in the standby mode to balance the voltage of fuel cell bus in transients due to the slow dynamic response of the fuel cell. The system is connected to the residential load and grid via a single phase bi-directional inverter and is designed to supply a 4.5 kW residential load. Two digital signal processors (TMS320F28335) are used to control the dc-dc converters and inverter at the device level and the system level control and energy management, are performed by a PC system. To control the power flow from the PV and fuel cell ports to the inverter port, the voltages of port two and three are shifted respected to the port one by leading phase angles of φ_{21} and φ_{31} respectively.

In the PV port, the switching devices of H-bridge dc-ac converter are shared with an interleaved current-fed boost converter. The interleaved boost converter is used to maintain the maximum power point tracking (MPPT) through duty ratio control while the dc-bus voltage regulation is carried out by

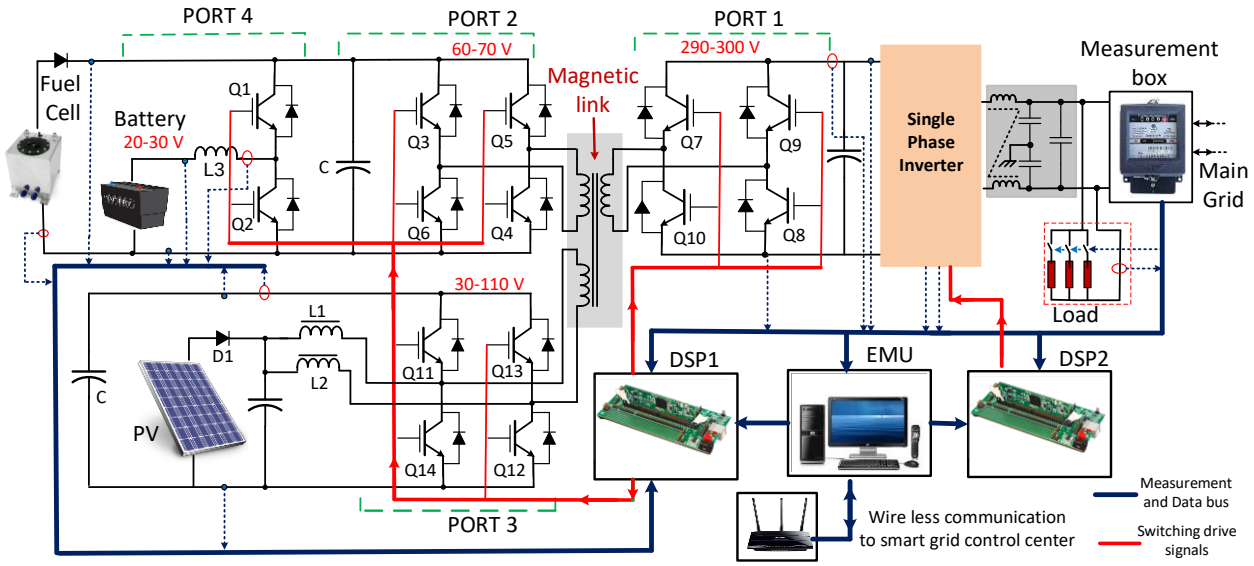

Fig.3. Schematic of the proposed residential micro-grid

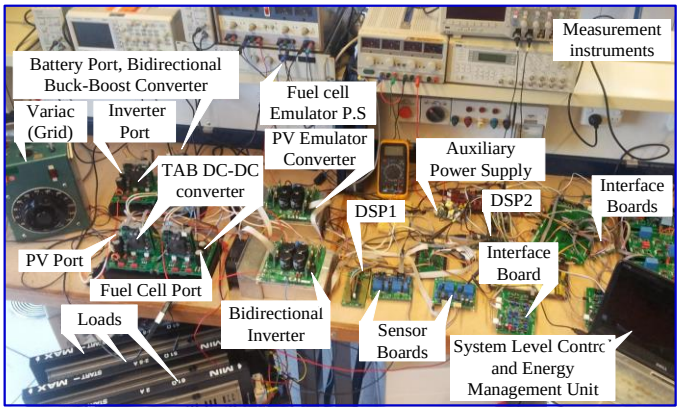

Fig.4. Experimentally developed residential micro-grid

using the phase shift angle φ_{31}. The voltage on the PV port changes reversely with the duty ratio to keep the equal volt-seconds on all three windings of the magnetic link and guarantees the ZVS operation of TAB converter ports. The proposed micro-grid can operate in various operation modes based on the power flow directions and active ports. The magnetic link facilitates the operation of the system in different modes with various energy management scenarios under both grid-connected and islanded conditions. More details on the system operation will be published in the future works and this study is focused on the copper loss analysis of the magnetic link.

III. Copper Loss Analysis Method

Due to the linear behaviour of copper, conduction loss analysis is carried out based on the harmonic contents of the currents in the windings of the magnetic link [10], [13], [26], [27]. Therefore, the total copper loss can be defined by summation of resultant loss of each harmonic component of the current as following

$$P_{Cu} = \sum_{n=1}^{h} P_{Cu,n} \tag{1}$$

where $P_{Cu,n}$ is the resultant copper loss of the nth harmonic and h the number of harmonics that are effective in the loss analysis.

The skin and proximity effects on the windings resistance can be considered separately for copper loss analysis of each harmonic due to their orthogonality principle [31]. Their effect is modelled as a frequency-dependent resistance for each harmonic in the case of non-sinusoidal currents. Therefore, the resultant loss of the nth harmonic $P_{Cu,n}$, can be calculated by

$$P_{Cu,n} = \left(\frac{I_n}{\sqrt{2}}\right)^2 R_{ac,n} \tag{2}$$

where $R_{ac,n}$ is the ac resistance of the Litz-wire winding for the nth harmonic and I_n the peak value of the nth harmonic of the non-sinusoidal current in the winding. To calculate the copper loss using (1) and (2) for the proposed magnetic link, the analytical methods for calculating the equivalent ac resistance, $R_{ac,n}$, and the amplitude of each harmonic, I_n, are discussed in the following sections.

IV. Harmonic Based Analysis of Currents In The Magnetic Link

The winding leakage inductances of the magnetic link are the main elements of power transfer between the ports in the proposed TAB converter. A T-model configuration of the three-winding magnetic link can be obtained by referring the leakage inductances of windings two and three to winding one as the reference. The magnetizing inductance is not considered in the model as it has a negligible effect on the power transfer between the ports due to the high-frequency range of the applied voltages [6]. The resultant model then can be transformed to the equivalent Δ-model to obtain the simplified TAB converter model as presented in Fig.5 [6]. The dc-bus and H-bridge converters are replaced with an equivalent square wave ac source in the resultant model. The voltage of

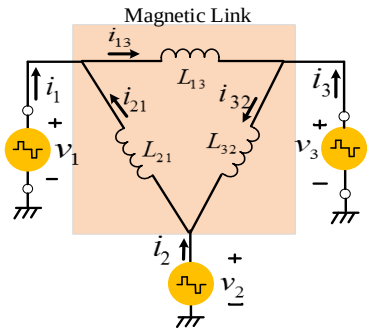

Fig. 5 The Δ-model equivalent circuit the three winding magnetic link

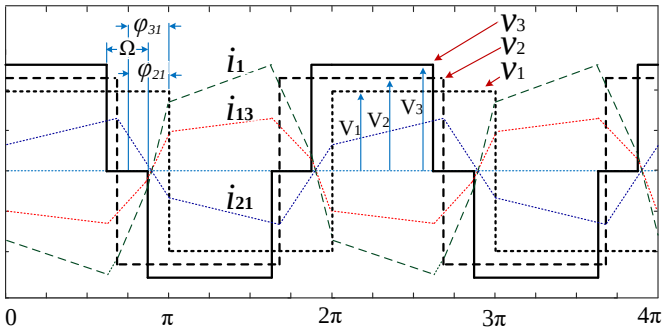

Fig.6 Voltage and current waveforms related to current i_1 in winding one

ports two and three are leading to port one (as the reference port) by phase shift angles, φ_{21} and φ_{31}, respectively as presented in Fig.6. This allows the power to transfer from the fuel cell and PV ports to the inverter port. A zero voltage angle, Ω, is introduced in the PV port ac voltage, v_3, to maintain the MPPT. Therefore, the amplitude of the dc voltage on the PV port, V_3, should be varied accordingly to maintain the ZVS operation as

$$V_3 = \frac{1}{1-(\Omega/\pi)} V_{3-\min} \tag{3}$$

where $V_{3\text{-}min}$ is the minimum value of the voltage on the PV port. The duty ratio, D, can be defined as

$$D = (1-\Omega/\pi) \tag{4}$$

In this paper, the duty ratio of the fuel cell and inverter ports is kept constant (D=1, Ω=0) due to the constant voltage of their buses.

A harmonic based analysis of non-sinusoidal currents is required to calculate the copper loss in the proposed magnetic link [13], [26], [27]. The winding currents are analyzed using the equivalent Δ-model. Therefore, the fundamental-harmonic phasor diagram of the currents and voltages in the equivalent Δ-model, presented in Fig.7, is used as the reference in the following analysis. The high-frequency square wave voltages illustrated in Fig.6 are represented based on their Fourier series as

$$\begin{aligned} v_1(t) &= \sum_{n=1}^{\infty} V_{1,n} \sin(n\omega t) \\ v_2(t) &= \sum_{n=1}^{\infty} V_{2,n} \sin(n(\omega t + \varphi_{21})) \\ v_3(t) &= \sum_{n=1}^{\infty} V_{3,n} \sin(n(\omega t + \varphi_{31})) \end{aligned} \tag{5}$$

where $V_{k,n}$ is the amplitude of the n-th harmonic of the voltage across winding k. For ports one and two, due to their constant amplitude, is defined as

$$V_{k,n} = \frac{2V_k(1-\cos(n\pi))}{n\pi}, \qquad k = 1,2 \tag{6}$$

For port three, due to the variable amplitude and duty ratio, it can be calculated by

$$V_{3,n} = \frac{2V_{3-\min}\cos(n\Omega/2)(1-\cos(n\pi))}{n(\pi-\Omega)} \tag{7}$$

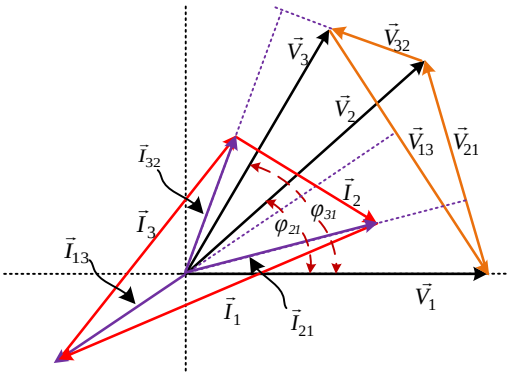

Fig.7 Fundamental phasor diagram of the TAB converter parameters

As can be seen in the equivalent model, i_1=i_{13}-i_{21}, i_2=i_{21}-i_{32} and i_3=i_{32}-i_{13}. Therefore, to analyze the current in winding one, i_1, the currents i_{21} and i_{13} should be calculated by using the voltage across inductors L_{21} and L_{13}. The voltage v_{21} can be calculated by using (5) as

$$v_{21}(t) = v_2(t) - v_1(t) = \sum_{n=1}^{\infty} V_{21,n} \cos(n\omega t + \alpha_n) \tag{8}$$

where $V_{21,n}$ is the amplitude of the nth harmonic, $v_{21,n}$, and is defined as

$$V_{21,n} = \sqrt{V_{1,n}^2 + V_{2,n}^2 - 2V_{1,n}V_{2,n}\cos(n\varphi_{21})} \tag{9}$$

and the phase angle of the nth harmonic, α_n, is calculated by

$$\alpha_n = \tan^{-1}\frac{V_{2,n}\sin(n\varphi_{21})}{V_{2,n}\cos(n\varphi_{21}) - V_{1,n}} \tag{10}$$

The current i_{21} can then be calculated taking into account π/2 as the inductive phase shift angle by

$$i_{21} = \sum_{n=1}^{\infty} I_{21,n} \sin(n\omega t + \alpha_n - \frac{\pi}{2}) \tag{11}$$

where $I_{21,n}$ is the amplitude of the nth harmonic, $i_{21,n}$, and can be calculated by

$$I_{21,n} = \frac{V_{21,n}}{(2\pi n f L_{21})} \tag{12}$$

Considering φ_{31} as the phase shift angle between v_3 to v_1, $I_{13,n}$ as the amplitude, and $(\beta_n$-$\pi/2)$ as the phase angle of the nth harmonic, the current, i_{13}, in the winding of L_{13} can be defined similarly to i_{21} as

$$i_{13} = \sum_{n=1}^{\infty} I_{13,n} \sin(n\omega t + \beta_n - \frac{\pi}{2}) \tag{13}$$

Finally, the *n*th harmonic of the current in the source v_1 and in the winding one of the magnetic link $i_{1,n}$ (refer to Fig.3) can be calculated by using (11) and (13) as

$$i_{1,n}(t) = i_{13,n} - i_{21,n} = I_{1,n}\sin(n\omega t + \psi_{1,n}) \tag{14}$$

where $I_{1,n}$, and $\psi_{1,n}$ are the amplitude and the phase angle of the *n*th harmonic of i_1 respectively and can be determined by

$$I_{1,n} = \sqrt{I_{13,n}^2 + I_{21,n}^2 - 2I_{13,n}I_{21,n}\cos(n(\beta_n - \alpha_n))} \tag{15}$$

$$\psi_{1,n} = \tan^{-1}\left(\frac{I_{13,n}\sin(n\beta_n) - I_{21,n}\sin(n\alpha_n)}{I_{13,n}\cos(n\beta_n) - I_{21,n}\cos(n\alpha_n)}\right) \tag{16}$$

The amplitude of each harmonic of the current in winding two, $I_{2,n}$, and the phase angle, $\psi_{2,n}$, and in winding three, $I_{3,n}$ and $\psi_{3,n}$, can be calculated similarly. It can be seen from (5) and (7) that v_1, v_2 and v_3 and consequently the resultant current in the windings only contain the odd harmonics. Once the harmonic contents of the current in the windings ($i_{1,n}$, $i_{2,n}$ and $i_{3,n}$) are determined, the ac resistance factor of each winding, $R_{ac,n}$, related to each harmonic term should be defined for loss analysis. Next section provides the details of calculating ac resistance.

V. Calculation of AC Resistance

The skin and proximity effects are considerable in medium and high-frequency applications. To reduce these effects, the twisted multi-strand enameled wires known as the Litz wire are commonly used. Considering these high-frequency effects, the ac resistance of a Litz wire winding is a function of frequency while the dc resistance is relatively constant and for each winding can be calculated by

$$R_{dc} = \frac{4Nl_s\rho_{Cu}}{n_s\pi d_{str}^2} \tag{17}$$

where N is the number of turns of a winding, l_s the average length of one turn, ρ_{cu} the resistivity of copper, d_{str} the strand diameter and n_s the number of strands.

The skin and proximity effect losses related to each harmonic of the current can be modeled through a frequency-dependent resistance, $R_{ac,n}$ [13]-[22]. The ratio of $R_{ac,n}$ to R_{dc} known as ac resistance factor, $F_{r,n}$, can be defined as

$$F_{r,n} = \frac{R_{ac,n}}{R_{dc}} \tag{18}$$

In the case of using Litz wires, the skin and proximity effects are appeared in both strand and bundle levels [18]. The bundle level proximity effect can be reduced effectively by twisting, while the bundle level skin effect needs more complex constructions [18] [25]. On the other hand, the strand level proximity effect is more considerable compared with the skin effects especially in the case of increasing number of layers [25]. The skin and proximity effects analysis in Litz wires are carried out based on two best-known analytical methods, the Dowell method, and Ferreira method. In the first method, the round conductors are replaced with the square conductors of the same area and then an equivalent foil conductor same as what Dowell analyzed is found. The one-dimensional field analysis is applied to the foil to find the losses [16]-[18].

The second approach is based on the field analysis of a single round conductor using the Bessel functions and some of its applications are proposed by Ferreira [19]-[22]. Both methods provide similar results and accuracy for small penetration ratios [13] although it has been shown that the second method provides more accurate results in high-frequency applications [22]. Both methods are reviewed in this paper briefly although the first method is used in this research due to the simplicity and relatively low switching frequency (10 kHz) and penetration ratio.

The first method is based on Dowell's equation for high frequency winding resistance of round conductors. The equation for the ac resistance factor, $F_{r,n}$, of the *m*th layer of round conductors is

$$F_{r,n} = \zeta_n\left[\upsilon_{1,n} + \frac{2(m^2-1)}{3}\upsilon_{2,n}\right] \tag{19}$$

where

$$\upsilon_{1,n} = \frac{\sinh(2\zeta_n) + \sin(2\zeta_n)}{\cosh(2\zeta_n) - \cos(2\zeta_n)}\ ,\ \upsilon_{2,n} = \frac{\sinh(\zeta_n) - \sin(\zeta_n)}{\cosh(\zeta_n) + \cos(\zeta_n)} \tag{20}$$

$$\zeta_n = (\frac{\pi}{4})^{0.75}\frac{d}{\delta_n}\sqrt{\eta}\ ,\ \ \eta = \frac{d}{p} \tag{21}$$

η is the porosity factor of round conductor, d the conductor diameter, and p the distance between centers of two adjacent conductors. The skin depth of round conductor of the *n*th harmonic, δ_n, is defined by

$$\delta_n = \sqrt{\frac{\rho_{Cu}}{\pi\mu_0 nf}} \tag{22}$$

where μ_o is the permeability of free space and f the frequency of the waveform. The simplified equation for $\zeta_n \le 2$ can be found [15] as

$$F_{r,n} \approx 1 + \frac{(5m^2-1)}{45}\xi_n^4 \tag{23}$$

The round conductor equation (19) is adapted to the Litz wire applications by replacing the number of layers m and the penetration ratio ζ_n with the effective number of Litz wire layers m_l and $\zeta_{str,n}$ from

$$m_l = m\sqrt{n_s} \tag{24}$$

and

$$\zeta_{str,n} = (\frac{\pi}{4})^{0.75}\frac{d_{str}}{\delta_n}\sqrt{\eta_{str}} \tag{25}$$

where η_{str} is the porosity factor of Litz wire [17].

In the second method (proposed in 1966), the skin and proximity effect losses of an isolated solid round conductor were evaluated using an exact solution of the internal and external magnetic fields [19] and further developed by Ferreira in 1990 [25], [31]. The closed form expression considering orthogonality of skin and proximity effects can be written as

$$F_{r,n} = \frac{\gamma_n}{2}\left[\tau_{1,n} - 2\pi\frac{4(m^2-1)}{3}\tau_{2,n}\right] \tag{26}$$

with

$$\tau_{1,n} = \frac{ber(\gamma_n)bei'(\gamma_n) - bei(\gamma_n)ber'(\gamma_n)}{ber'(\gamma_n)^2 + bei'(\gamma_n)^2} \tag{27}$$

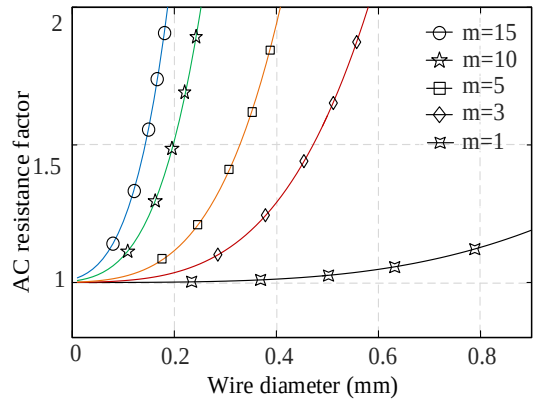

(a)

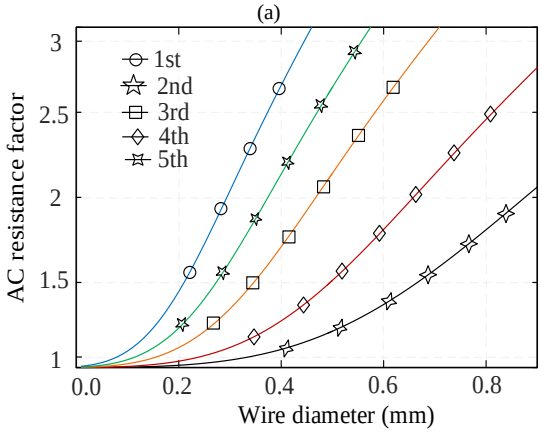

(b)

Fig.8 AC resistance factor as a function of wire diameter for: (a) different number of winding layers, and (b) various harmonics of the current in windings of the magnetic link

$$\tau_{2,n} = \frac{ber_2(\gamma_n)ber'(\gamma_n) + bei_2(\gamma_n)bei'(\gamma_n)}{ber'(\gamma_n)^2 + bei'(\gamma_n)^2} \tag{28}$$

where *ber* and *bei* are the real and imaginary parts of the first kind Bessel function and γ_n is the round conductor penetration ratio of the *n*th harmonic defined as

$$\gamma_n = \frac{d}{\delta_n\sqrt{2}} \tag{29}$$

The accuracy of the resultant equation later was improved by introducing a porosity factor as a correction for the magnetic field in (26) [32]. In the case of Litz wires, the skin and internal proximity effects were already determined in [19] based on the solid round conductor analysis presented in (26) and further improvements were applied by Ferreira [31]. To improve the accuracy in high-frequency applications, an expression was also introduced using exact Bessel functions [22]. The reduced expression applicable to low penetration ratios can be expressed as

$$F_{r,n} = \left[1 + \frac{\gamma_n^4}{192}\left(\frac{1}{6} + \frac{\pi^2 n_s p_f}{4}(16m^2 - 1 + \frac{24}{\pi^2})\right)\right] \tag{30}$$

with

$$P_f = n_s(r_s / r_b)^2 \tag{31}$$

where P_f , r_s and r_b are the packing factor, strand radius and bundle radius of Litz wire, respectively, and $\tau_{1,n}$ and $\tau_{2,n}$ are approximated by the first terms of their Taylor-series [21] as the following

$$\tau_{1,n} = \frac{2}{\gamma_n} + \frac{(\gamma_n)^3}{96} - \frac{(\gamma_n)^5}{3072} + \ldots \approx \frac{2}{\gamma_n} \tag{32}$$

$$\tau_{2,n} = -\frac{(\gamma_n)^3}{16} + \frac{(\gamma_n)^7}{512} + \ldots \approx -\frac{\gamma_n^3}{16} \tag{33}$$

This approximation for low penetration ratios ($\gamma_n < \sqrt{2}$) is acceptable due to the utilization of Litz wires. Although the reduced equation (30) has presented good results for low penetration ratios, it loses its accuracy for higher values of penetration ratio. In [20], two porosity factors were applied to the equation to improve the accuracy. In [21], the external field of each strand is considered precisely and a more accurate equation was achieved.

It has been shown that the dc and ac resistances and consequently copper loss are tightly coupled to the temperature [33]-[35]. The dc and low-frequency resistance R_{dc} is affected by temperature due to the change in the copper resistivity ρ_{Cu}. Applying a temperature variation component $[1+\alpha(T-T_0)]$ the copper resistivity in (17), results in the following equation for dc and low-frequency resistance.

$$R_{dc,T} = R_{dc,T_0}(1 + \alpha(T - T_0)) \tag{34}$$

where T_0 is the reference temperature (normally 20 °C), T the actual winding temperature and α is the temperature coefficient of resistivity (for copper is 3.93×10^{-3} K^{-1}). On the other hand, the ac resistance R_{ac} is affected by the temperature in a different way due to the variation of both resistivity and penetration ratio. The ac resistance factor ($F_{r,n}$) for each harmonic content by applying the temperature variation element to the resistivity in (22)-(23) and doing some arrangement is obtained as

$$F_{r,n,T} = 1 + \frac{F_{r,n,T_0} - 1}{[1 - \alpha(T - T_0)]} \tag{35}$$

where $F_{r,n,T0}$ is the ac resistor factor at the reference temperature T_0 [33]. Therefore, the ac resistance as a function of temperature for *n*th harmonic of the windings current can be found as

$$R_{ac,n,T} = R_{dc,T}F_{r,n,T} = R_{dc,T_0}\left[1 + \alpha(T - T_0) + \frac{F_{r,n,T_0} - 1}{1 + \alpha(T - T_0)}\right] \tag{36}$$

More details on the temperature effects on the estimated copper loss and accuracy improvement techniques can be found in [33]-[35].

In this paper, the copper loss of the magnetic link is calculated based on the first method by using (19)-(25).

VI. Copper Loss Evaluation Of The Magnetic Link

This section reviews the copper loss calculation of the magnetic link considering all effective elements. As can be seen in (19)-(21), the harmonic frequency, strand diameter and number of winding layers have major effects on the ac resistance factor and consequently the copper loss. Fig.8 (a) illustrates the effect of increasing number of winding layers on the ac resistance factor. As can be seen the ac resistance of wire decreases by reducing the number of windings layers and using strands of less diameter. Fig.8 (b) shows the ac resistance factor, $F_{r,n}$ for the five major harmonics of the converter currents. It can be seen that the ac resistance factor

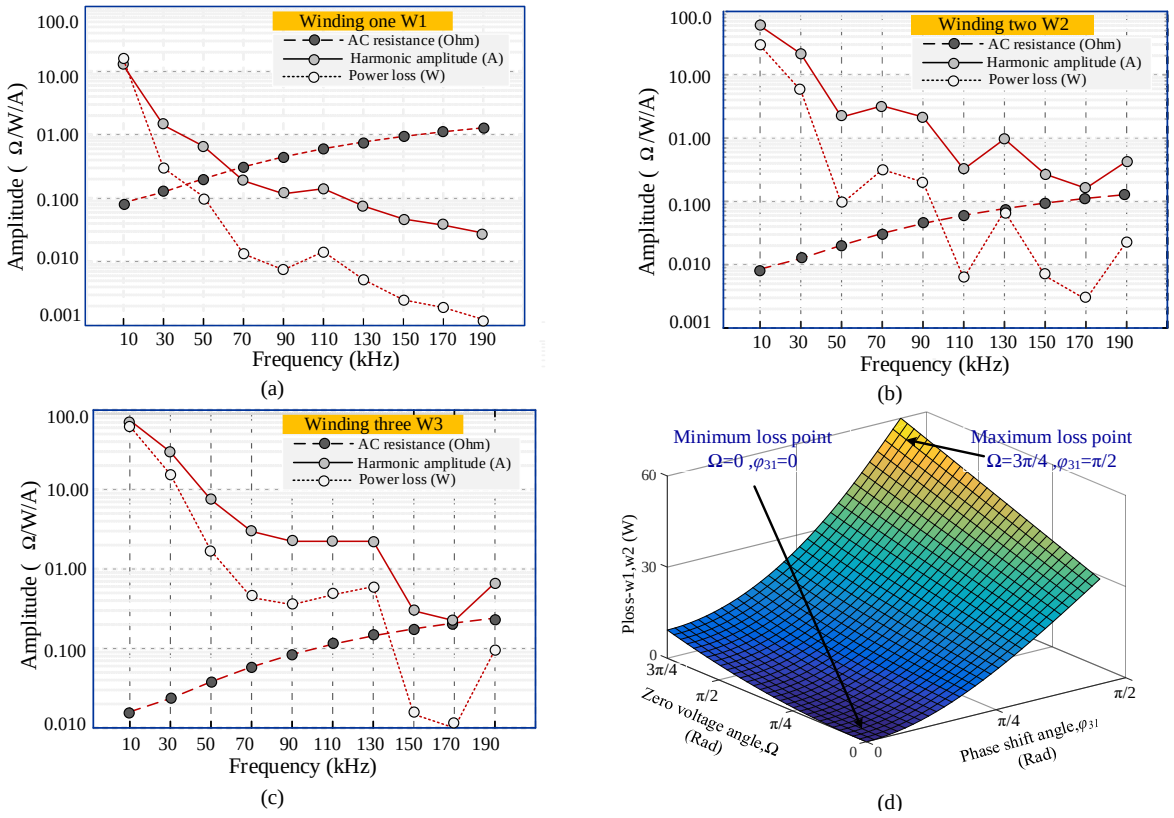

Fig.9 AC resistance, harmonic amplitude and copper loss of (a) winding one (W1), b) winding two (W2) and three winding three (W3) and (d) conduction loss of the windings one and three for zero voltage angle, Ω=0 to 3π/4 and φ_{31}= 0 to π/2

decreases for lower harmonic orders and smaller strand diameters. Therefore, reducing the operating frequency can reduce not only the switching loss but also the winding losses in the converters.

A. Calculation of maximum copper loss

The maximum copper loss is important in the optimal design and thermal analysis of the magnetic link. According to the power flow equation of TAB converter, maximum power flow and RMS current in the magnetic link take place when the fuel cell and PV ports are transferring the maximum power (φ_{21}=π/2, φ_{31}=π/2)[4]-[7]. On the other hand, when the PV bus voltage, V_3, is maximized and the duty ratio, D, is minimized, the amplitude of the fundamental component of the current in winding three increases and raises the loss. Therefore, the duty ratio is equal to its minimum value when the copper loss in winding three is maximized (D=0.25 and Ω=3π/4 in this case). The power losses of all windings were analytically calculated for the specified operation point and integrated to define the maximum copper loss of the magnetic link.

To consider the temperature effect, the copper loss is primarily calculated at the reference temperature. The actual temperature then is estimated assuming an almost linear relation between temperature and copper loss and proportionality of copper loss to the square of the output power, taking into account the maximum target temperature. Using this method avoids the computationally expensive finite element methods although, comparing the resultant losses and estimated steady-state temperatures to the experimentally measured values showed less than 10 % error. Finally, the simulations based on the analytical method have been repeated using the measured values of temperature to cancel the error resulted from estimated temperatures. Fig.9 illustrates the calculated value of ac resistance, $R_{ac,n}$, the amplitude of harmonic I_n , and the resultant copper loss, $P_{cu,n}$, of each current harmonic in the windings. As can be seen, the copper loss is decreased when the harmonic orders increase as the effect of reduction in harmonic amplitude overcomes the increasing ac resistance. The calculated value of copper losses of windings one, two and three by using (1) are equal to 16 W, 35 W, and 72 W, respectively. Therefore, the maximum copper loss of the magnetic link in this operation mode is 130 W.

B. Loss analysis under phase shift angle and duty ratio variation

To study the effect of variation of phase shift angle, φ_{31}, and zero voltage angle, Ω, of the PV port on the copper loss, two common operation modes have been considered.

In the first operation mode, only the PV and inverter ports are active and the dc-dc converter operates in the DAB mode. The phase shift angle, φ_{31}, was changed from 0 to π/2 and the zero voltage angle, Ω, from 0 to 3π/4 (assuming that the voltage of PV port varies from 30 V to 120 V). Fig.9-(d) presents the copper loss of the magnetic link for the entire operation range calculated by the method outlined in section III. It can be seen that in general any increase in the phase shift angle and zero voltage angle increases the copper loss

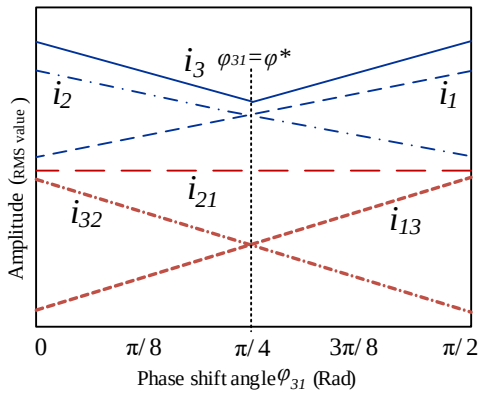

Fig.10. Trends of the winding currents in the magnetic link versus phase shift angle

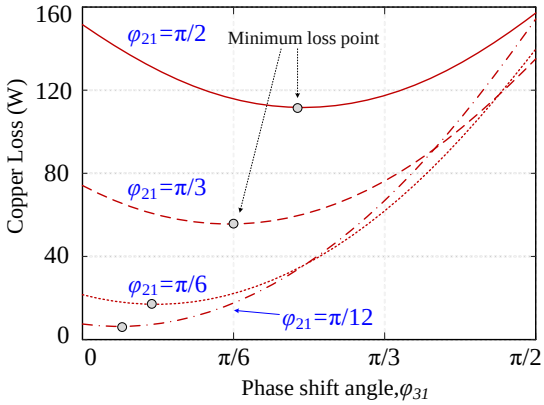

Fig.11. Copper loss of magnetic link for different values of φ_{21} and φ_{31}

although the effect of phase shift angle is more considerable compared to that of zero voltage angle. Increasing the zero voltage angle at higher phase shift angles raises the amplitude of current fundamental component in the PV port which results in more effect on the copper loss at higher phase shift angles. As expected, the maximum loss takes place at $\varphi_{31}=\pi/2$ and $\Omega=3\pi/4$, which is about 62 W.

In the second case, the converter operated in the TAB mode and both fuel cell and PV ports were active and transferred power to the inverter port. The fuel cell port was operated with constant phase shift angle and duty ratio ($\varphi_{21}=\pi/2$, $\Omega=0$) due to the constant bus voltage. At the PV port, the bus voltage, V_3, zero voltage angle, Ω, and the phase shift angle, φ_{31}, have been changed similar to the previous stage.

Fig.10 illustrates the overall trend of the currents in the equivalent Δ-model (i_{21}, i_{13} and i_{32}) and in the windings (i_1, i_2 and i_3) with the variation of phase shift angle, φ_{31}. As can be seen increasing φ_{31} raises i_{31} and the power transferred from PV to the inverter while i_{21} remains constant due to the constant value of φ_{21}. On the other hand, increasing φ_{31} reduces φ_{23} (as $\varphi_{23}=\varphi_{21}-\varphi_{31}$) and i_{32} and consequently the power transferred from the fuel cell port to the PV port. Refereeing to the Δ-model nodal equations ($i_1=i_{13}-i_{21}$, $i_2=i_{21}-i_{32}$, and $i_3=i_{32}-i_{13}$), one can see that when φ_{31} increases, i_1 and consequently the copper loss in winding one increases while i_2 and the copper loss in winding two decreases. In winding three, i_3 decreases for phase shift angles less than $\pi/4$ and then increases. This is because, for small phase values of φ_{31}, the power received from port two is more than power transferred to port one. At $\varphi^*_{31}=\varphi_{21}/2=\pi/4$ the power received from port two and transferred to port one are almost equal. Therefore, the average power of the port and the current i_3 are minimized at this point, and the copper loss of winding three and the total copper loss of the magnetic link are minimized at this point. As can be seen in Fig.11, the minimum loss point where $\varphi_{31}=\varphi^*_{31}$ depends on φ_{21} and always $\varphi^*_{31}=\varphi_{21}/2$ where the received and transferred powers to the port three are equal. Fig.12 presents the resultant winding copper losses and the total loss versus the phase shift angle, φ_{31}, and zero voltage angle, Ω. As shown in Fig.12 (a)-(b), increasing the phase shift angle, φ_{31}, raises the loss in winding one and decreases the average power, current and loss of winding two. As presented in Fig.12 (c)-(d), the copper loss of winding three and the total loss are minimized at $\varphi_{31}=\varphi^*=\pi/4$ due to the previous discussions.

VII. Experimental Tests And Validation

A prototype of the proposed micro-grid including three port phase shift dc-dc converter and the high-frequency magnetic link was developed as presented in Fig.4. The waveforms of the TAB converter for the case of D= 1, $\varphi_{31}=\pi/3$ and $\varphi_{21}=\pi/5$ is presented in Fig.13 and the micro-grid parameters are presented in Table.II/Appendix. To reduce the skin and proximity effects, Litz wires with the strand diameter of 0.35 mm (27 AWG) are used. The number of twisted isolated strands for windings one, two and three were chosen as 17, 42 and 28 and their number of turns resulting from the design process was 48, 11 and 16 turns, respectively.

A. Measurement of copper loss for DAB and TAB operation modes

To measure the conduction loss of the magnetic link, an experimental test platform was established. The current and the voltage waveforms are measured by Tektronix current measurement probe TCPA300 and high-voltage differential probe P5200, respectively. The power was measured by a power analyzer PM3000A and the ac resistances of windings, related to each of the harmonics is measured by using an Instek LCR meter. To validate the analytical methods, a series of experimental tests were conducted for two cases of operation modes discussed in section VI. To study the effects of phase shift and zero voltage angle variations on the total copper loss of the magnetic link, the copper loss was measured for the DAB and TAB operation modes and the measured values are compared with the analytically calculated results. Fig.14 shows the theoretically calculated and experimentally measured values of the ac resistance of windings one, two and three for a frequency range of 10-190 kHz. As can be seen, the measurement error increases for higher frequencies although it remains less than 5% for the entire measurement range. On the other hand, the amplitudes of current harmonics in each

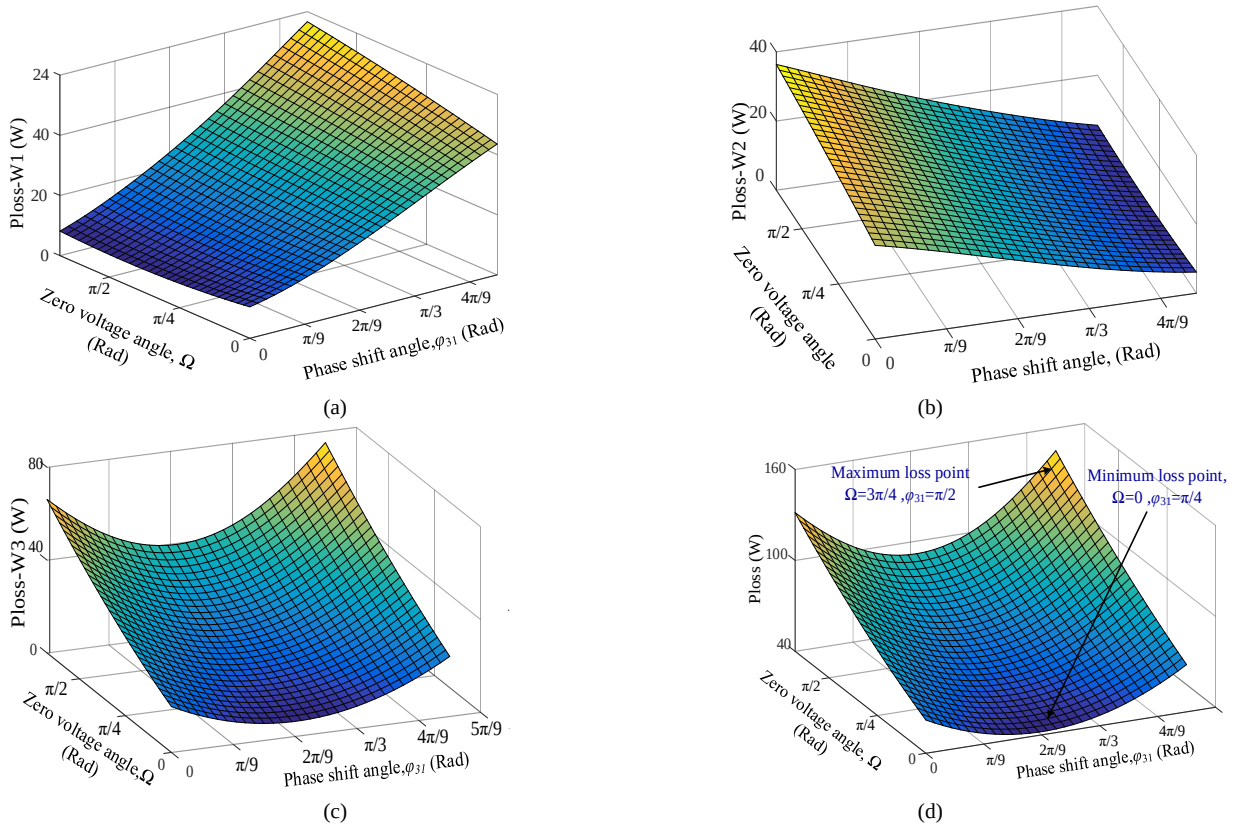

Fig.12 Copper loss of the magnetic link where Ω=0 to 3π/4 and φ_{31}= 0 to π/2, (a) winding one (W1), (b) winding two (W2), (c) winding three (W3), and (d) total magnetic link

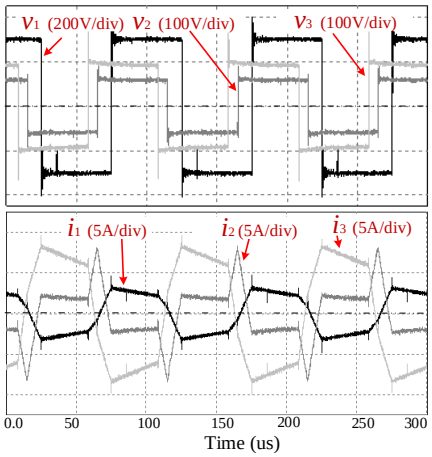

Fig.13. The experimentally measured waveforms of the TAB converter for D= 1, φ_{31} = π/3, and φ_{21} = π/5

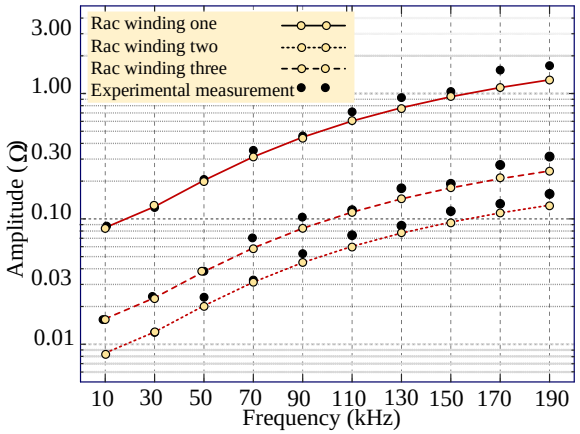

Fig.14. Calculated and measured values of resistances of the windings of magnetic link

winding are measured and compared with the theoretical values for a similar frequency range as presented in Fig.15. As can be seen in the figure, the measured values of the harmonic amplitudes of the current in all three windings of the magnetic link presented same trends as analytically calculated results. The error between measured and calculated values for higher frequency harmonics is slightly increased due to the small amplitude of the harmonics and limited accuracy of the measurement system (spectrum analyser) which is not important due to negligible impact of those harmonics on the copper loss. The measured values of ac resistance and harmonic amplitude of each harmonic term are used to calculate the copper loss attributed to that harmonic and the total copper loss of that winding by using (1) and (2). In the DAB operation mode, the effect of variation in zero voltage angle from 0 to π/2 was experimentally measured for two cases of phase shift angles, such as φ_{31}= π/8 and φ_{31}=π/2. The measured values are compared with analytically calculated values (discussed in section VI-*B*). The comparison result is illustrated in Fig.16 (a). It can be seen that the experimental result validates the analytical calculations although the resultant error increases at lower values of conduction loss and higher zero voltage angles which can be attributed to the accuracy of measurement instruments.

In the case of TAB operation mode, the effect of phase shift angle variation on copper loss was tested for analytically

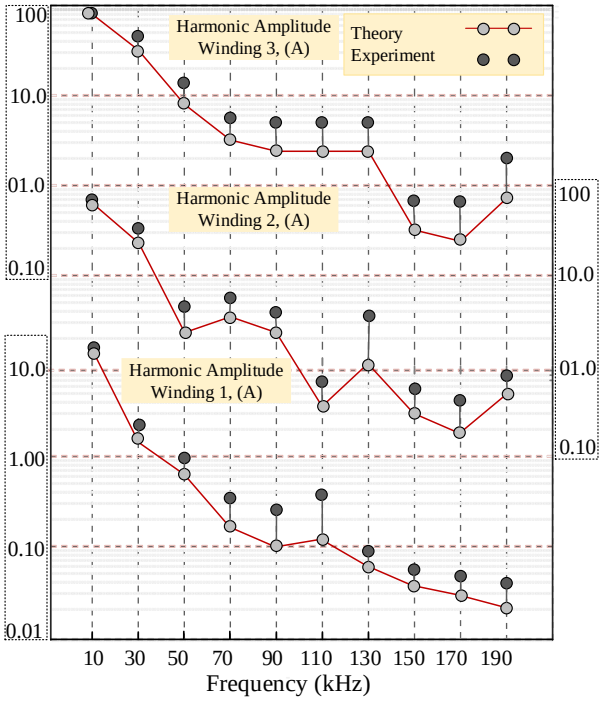

Fig.15. Calculated and measured values of harmonic amplitudes of the currents in each winding of the magnetic link

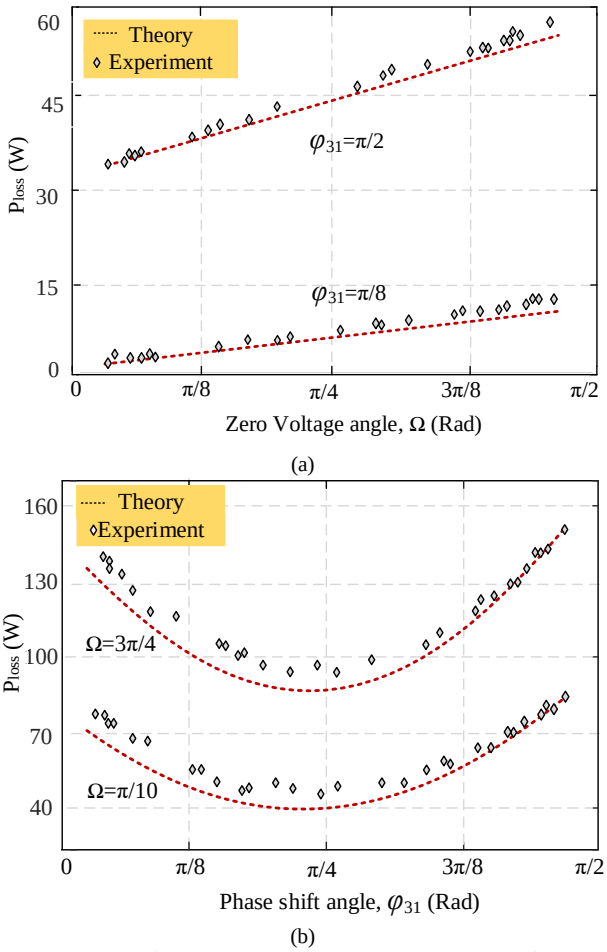

Fig.16.Comparison of calculated and measured conduction loss for (a) DAB mode (Ω= 0- π/2, φ_{31}= π/8 and φ_{31}=π/2), and (b) TAB mode, (φ_{21}=π/2, φ_{31}= 0-π/2, Ω= π/10 and Ω= 3π/4)

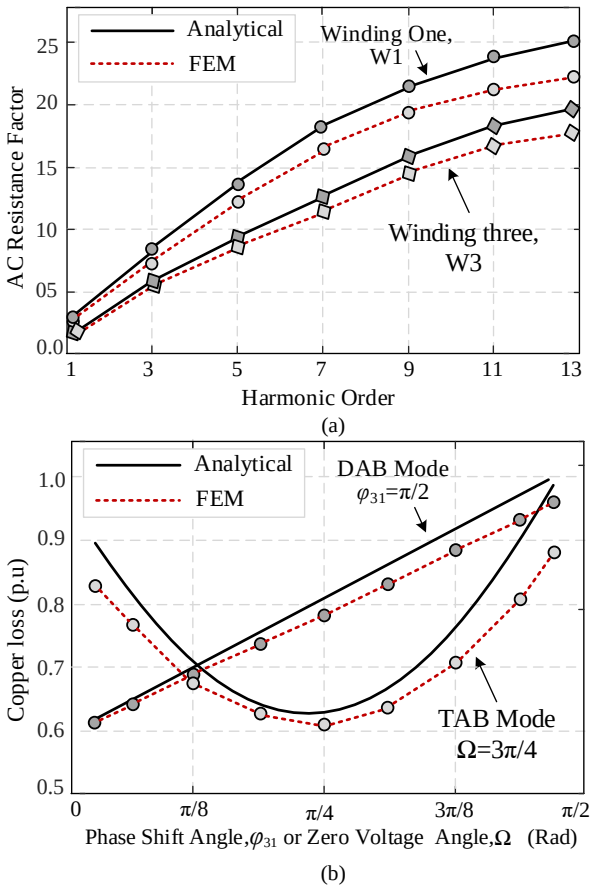

Fig.17. (a) The ac resistance factor as a function of harmonic order of currents in windings one and two based on Dowell analytical method and FEM, and (b) normalized copper loss for DAB operation mode versus zero voltage angle and TAB operation mode versus phase shift angle.

calculated values in section VI-*B*. The total copper loss of the magnetic link was measured for two cases of Ω= π/10 and Ω= 3π/4 (maximum loss) where φ_{21}=π/2 and φ_{31} were changed from 0 to π/2. As is presented in Fig.16(b), experimentally measured losses showed same trends as the calculations and the total loss of the magnetic link is minimized at φ_{31}=π/4 as discussed in section VI. The resultant error is about 10% at lower phase shift angles and reduces to less than 5% for higher phase shift angles.

To study the edge effects of the magnetic link on the ac resistance of the windings and the total calculated copper loss, finite-element method (FEM) simulations are carried out. The ac resistance factor (F_r) attributed to each individual harmonic of the current in the windings of the magnetic link is calculated numerically considering a 2D model of the magnetic link using ANSYS Maxwell. The resultant values of the ac resistance factor according to the harmonic order for each winding are calculated and compared to the analytically calculated ones as presented in Fig.17 (a) for windings one and three. It was seen that the FEM based results are smaller than the analytical values for the all harmonic contents and the difference increases for higher order harmonics. On the other hand, the total copper loss for each operating point was defined by summation of the copper losses of all harmonic contents. The process is performed for both DAB and TAB operating modes and the results are compared with the

TABLE I

EQUATIONS THAT ARE USED TO DEFINE THE PARAMETERS OF THE MAGNETIC LINK

Test Parameter	Differentially coupled and open circuit tests	Cumulatively coupled and open circuit tests	Combination of all three tests
R_{W1}	$\frac{(2N_{31}-1)R_1(OC)-R_3(OC)+R_{13}(dif)}{2N_{31}}$	$\frac{(2N_{31}+1)R_1(OC)+R_3(OC)+R_{13}(cum)}{2N_{31}}$	$R_1(OC)-\frac{R_{13}(cum)-R_{13}(dif)}{4N_{31}}$
R_{W3}	$\frac{(2-N_{31})R_3(OC)-N_{31}R_1(OC)+N_{31}R_{13}(dif)}{2}$	$\frac{(2+N_{31})R_3(OC)+N_{31}R_1(OC)-N_{31}R_{13}(cum)}{2}$	$R_3(OC)-\frac{N_{31}R_{13}(cum)-N_{31}R_{13}(dif)}{4}$
R_m	$\frac{R_3(OC)+R_3(OC)-R_{13}(dif)}{2N_{31}}$	$\frac{R_{13}(cum)-R_1(OC)-R_3(OC)}{2N_{31}}$	$\frac{R_{13}(cum)-R_{13}(dif)}{4N_{31}}$
L_{l1}	$\frac{(2N_{31}-1)L_1(OC)-L_3(OC)+L_{13}(dif)}{2N_{31}}$	$\frac{(2N_{31}+1)L_1(OC)+L_3(OC)-L_{13}(cum)}{2N_{31}}$	$L_1(OC)-\frac{L_{13}(cum)-L_{13}(dif)}{4N_{31}}$
L_{l3}	$\frac{(2-N_{31})L_3(OC)-N_{31}L_1(OC)+N_{31}L_{13}(dif)}{2}$	$\frac{(2+N_{31})L_3(OC)+N_{31}L_1(OC)-N_{31}L_{13}(cum)}{2}$	$L_3(OC)-\frac{N_{31}L_{13}(cum)-N_{31}L_{13}(dif)}{4}$
L_{13}	$\frac{L_1(OC)+L_3(OC)-L_{13}(dif)}{2N_{31}}$	$\frac{L_{13}(cum)-L_1(OC)-L_3(OC)}{2N_{31}}$	$\frac{L_{13}(cum)-L_{13}(dif)}{4N_{31}}$

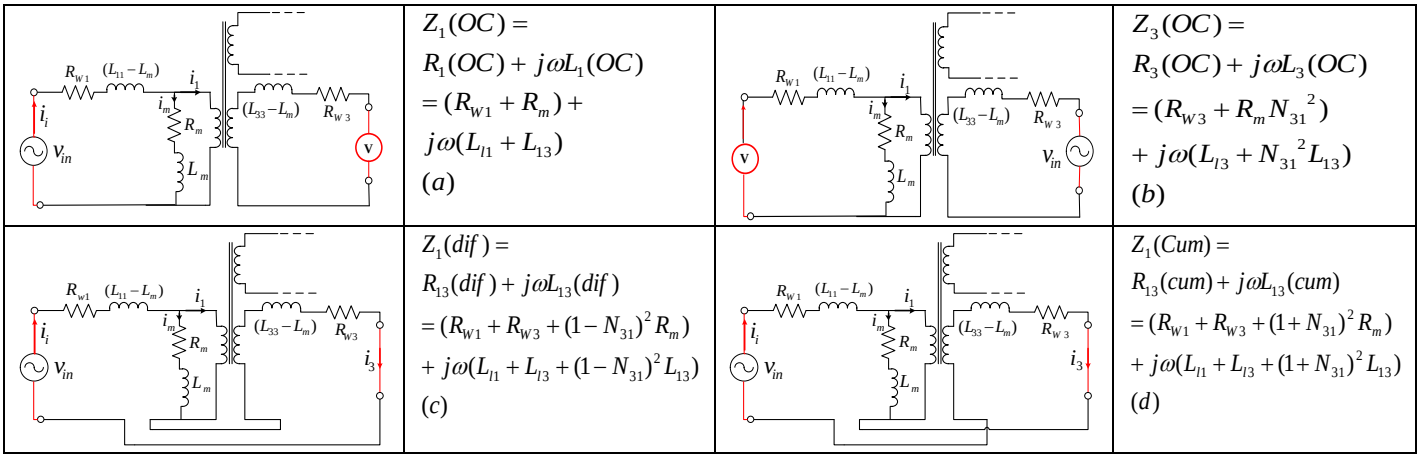

Fig.18. Experimental tests of magnetic link and related equations (a) secondary open circuit test, (b) primary open circuit test, (c) series coupling-differentially coupled test, and (d) series coupling-cumulatively coupled test.

simulations as presented in Fig.17 (b). As can be seen, the results are almost close while the analytical method based on the Dowell's equation overestimates the losses between 5-10 % (due to the edge effects) depending on the zero-voltage angle (**Ω**) and phase shift angles (φ_{21} and φ_{31}) range.

B. Measurement of the parameters of the magnetic link

Due to the dependency of the currents in the windings of the magnetic link to the leakage inductances, there is a need to measure the leakage inductances of the windings as a function of harmonic frequencies. The conventional short and open-circuit tests lose their accuracy in the case of the large value of leakage inductances where the effect of the magnetizing inductance cannot be ignored or in the case of unequal primary and secondary leakage inductances or winding resistances [5],[36]. In these cases, the series-coupling tests are recommended due to their accuracy as the primary and secondary windings of the transformer are connected electrically (referred to Fig8). Therefore, to increase the accuracy of the measurements, a combination of open-circuit and the differentially and cumulatively coupled tests are used as presented in Fig.18. The advantage of the series-coupling measurements over the open- and short-circuit tests is that the series-coupling tests can additionally be used to factor in the effects on the magnetizing and leakage inductances of the core excitation [36]. Furthermore, the resistances and inductances measured in the series-coupling tests are the algebraic addition and subtraction of resistances and inductances in the transformer, thus facilitating direct measurement by the meter [34]. The tests are performed only for the main harmonic frequencies (first five harmonics) and the measurements are applied to each pair of the windings while the third winding was open-circuited as presented in Fig.18. The impedances including separated real and imaginary parts are measured.

To find the final value of the parameters related to each frequency, a combination of series-coupling and the open-circuit test results are used based on equations presented in table I, where N_{31} is the turns ratio of the winding three to winding one ($=N_3/N_1$), R_{w1} and R_{w3} the ac resistances of

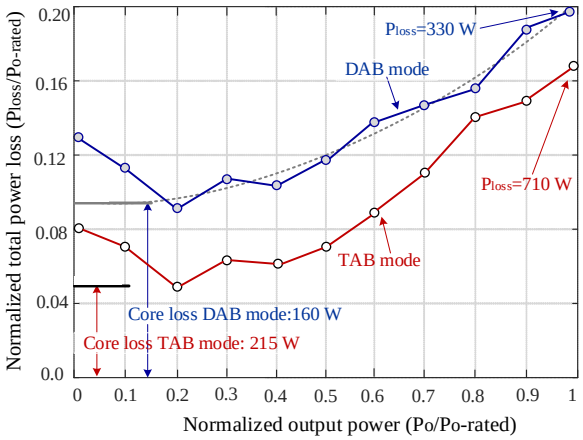

Fig.19. The normalized total power loss of the converter for DAB and TAB operation modes

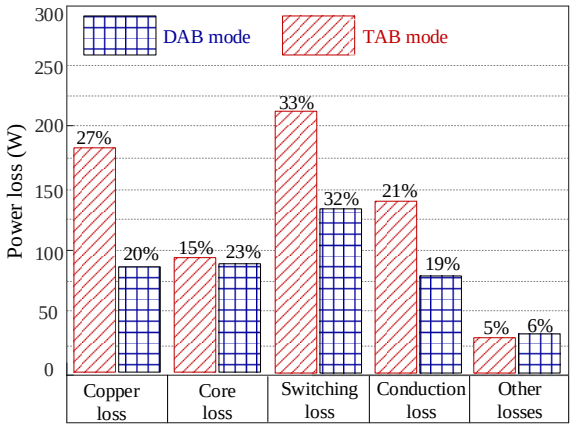

Fig.20. Power loss breakdown of the converter

windings one and three respectively and R_m the core loss equivalent resistance. L_{l1}, L_{l3} and L_m are the leakage inductances of winding one and three and magnetizing inductance respectively. The average of the cumulative and differential coupled and the open-circuit tests show excellent correlation compared to the short-circuit test (maximum of 8% standard deviation). Therefore, averaging the resultant values from tabulated equations estimates the parameters with acceptable accuracy for each particular harmonic frequency. It was seen that the measured leakage inductances slightly decreased for higher harmonics due to the proximity effects although the differences were negligible due to the range of the harmonic frequency (less than 100 kHz).

C. Loss breakdown of the proposed micro-grid

The copper loss of the magnetic link for two cases of DAB and TAB operation modes for a wide range of output power was measured. The resultant value of the copper loss is used to obtain the loss breakdown profile of the dc-dc converter for both operation modes. The overall power loss of the converter for each operation mode is obtained by measuring the difference between the input and output powers.

In general, the overall power loss can be divided into five components: the copper and core losses of the magnetic link, the switching and conduction losses in the switching devices and the stray power loss. The copper loss is measured on a

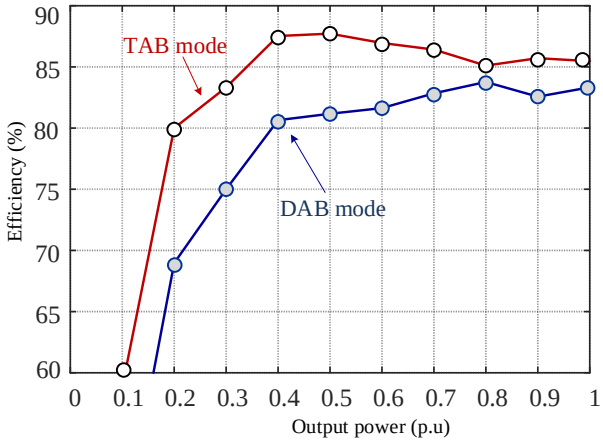

Fig.21. Converter efficiencies for DAB and TAB operation modes versus normalized output power

harmonic basis by using the proposed method in the previous sections. The core loss of the converter for each operation mode (DAB or TAB) can be obtained from the power loss curves. The total loss of the converter for a complete range of output power in both DAB and TAB modes is normalized to the rated value of output power ($P_{\text{O,rated-DAB}}$=1650 W, $P_{\text{O,rated-TAB}}$=4300 W) and presented in Fig.19. The overall loss data can be fitted with a third-order polynomial in the ZVS operation region [37]. The overall core loss is obtained by extrapolating the fitted polynomial curve to the vertical axis at zero output power. This is because the copper loss is almost zero at no-load condition neglecting the small copper loss due to the magnetizing current of the magnetic link. This is because the converter produces this power loss even at zero output power if it is possible to extend the ZVS operation to the entire range of output power [37]. As can be seen, the core losses for the DAB and TAB modes are obtained as 160 W and 215 W, respectively.

A majority of switching loss in the converter is attributed to the turn-off switching time as the converter operates at ZVS during turn-on switching times. The switching loss is proportional to the switching frequency, f_s, and the square of the turn-off switching current, I_{sw}, and is calculated based on the method presented in [37]. The conduction loss, P_{con}, in the switching devices is calculated using the measured values of current and device datasheet by [38], [39]

$$P_{con} = V_{CEO} I_{C,avg} + R_{ce,ON} I_{C,rms}^2 \quad (37)$$

where V_{CEO} is the IGBT on-state zero-current collector-emitter voltage drop and $R_{ce,ON}$ the IGBT collector-emitter On-state resistance obtained from the IGBT datasheet [40]. The average current, $I_{C,avg}$, and the RMS current, $I_{C,rms}$, of the IGBT are obtained from the experimental measurement. There are some stray losses which can be obtained by subtracting the copper loss, core loss, switching loss, and conduction loss from the total value of measured power loss. Fig.20 illustrates the power loss breakdown of the converter for both operation modes. As can be seen, the core loss in the TAB mode accounts for about 30 % of the total loss while it increases to 45 % for the DAB converter. The reason is that the magnetic link is designed according to the converter power rating in the TAB operation mode (4.5kW). Therefore, the dc-dc converter operates with less efficiency in the DAB mode. Fig.21

illustrates the converter efficiency for the DAB and TAB operation modes for a complete range of output power. As can be seen, the highest efficiency in the TAB mode is about 87.5% at P_o=0.4*$P_{TAB,rated}$ and it reduces to 85.5% at the rated power (4300 W). On the other hand, in the DAB mode, the efficiency increases for higher output power from 60% at P_o=0.1*$P_{DAB,rated}$ to 84% at the rated power (1650W). It should be noted that the majority of the power loss is attributed to the core loss in both operation modes.

VIII. Conclusion

The copper loss of a multi-winding magnetic link based on the Dowell's equation which takes into account both the skin and the proximity effects, and the harmonic contents of the excitation waveforms has been presented. The phase shift angle, duty ratio and amplitude variation of the excitation voltages on the copper loss have been taken into account. The temperature effect on the ac resistance factor and the copper loss is studied, and it is estimated based on the proportionality to the square of the output power although, the resultant error was less than 10 %. It was seen that in the case of the DAB operation mode, any increase in the phase shift angle and zero voltage angle increases the copper loss although, the phase shift angle presented more impact. In the case of the TAB operation mode, when PV and FC transfer power to the inverter port, the copper loss is minimized when their leading phase shift angles are equal. Comparing analytical and experimental results showed that the analytical method provides better accuracy at higher phase shift and lower zero-voltage angles (error less than 5 %). The loss analysis also carried out using FEM to study the edge effects of the magnetic link on the ac resistance and copper loss. It was seen that the analytical method using Dowell's equation results in a 5-10% overestimate of the loss depending on the phase shift and zero-voltage angles range. The loss breakdown and efficiency range of the converter for both DAB and TAB operation modes are obtained. The cumulatively and differentially series coupling tests along with the open-circuit test have been used to define the dependency of inductive and resistive elements of the magnetic link to the harmonic frequencies.

APPENDIX

TABLE II
THEORETICAL AND EXPERIMENTAL PARAMETERS

Description	Value
Electrical Parameters	
Nominal power	4.5 kW
Nominal power of each winding	P_{W1}=4.5kW, P_{W2}=2.2kW, P_{W3}=2.8kW
Nominal windings voltage	V_{W1}=300±15 V, V_{W2}=60±3 V V_{W3}= 100±5 V
Number of turns	N1 : N2 : N3= 48 : 11 :16
Magnetic core	Ferrite-N87-EE
Operating frequency	10 kHz
Required leakage inductance	L_{l2}=26µH, L_{l1}=54µH,
Magnetizing inductance	L_{l3}=30µH, L_m= 64 µH
Loss Analysis Parameters	
Litz wire strand diameter	27 AWG / 0.35 mm
Resistivity factor of copper conductor	1.7*10.E-8 Ω.m
Conductivity of copper conductor	58.5*10.E+6 Siemens/m
DC resistance of windings (mΩ)	$R_{dc\text{-}w1}$=52, $R_{dc\text{-}w2}$=22, $R_{dc\text{-}w3}$=19
Permeability of copper conductor	1.256*10.E-6 $H.m^{-1}$
Maximum current density	4 $A.mm^{-2}$

REFERENCES

[1] Y. M. Chen, Y. C. Liu, and T. F. Wu, "Multi-input dc–dc converter based on the multi-winding transformer for renewable energy applications," *IEEE Trans. Ind. Appl.*, vol. 38, no. 4, pp. 1096–1104, July/August 2002

[2] M. R. Islam, G. Lei, Y. Guo and J. Zhu, "Optimal Design of High-Frequency Magnetic Links for Power Converters Used in Grid-Connected Renewable Energy Systems," *IEEE Trans. Magn.*, vol. 50, no. 11, pp. 1-4, Nov. 2014

[3] H. Tao, A. Kotsopoulos, J. L. Duarte and M. A. M. Hendrix, "Transformer-Coupled Multiport ZVS Bidirectional DC–DC Converter With Wide Input Range," *IEEE Trans. Power Electron.*, vol. 23, no. 2, pp. 771-781, March 2008

[4] H. Tao, A. Kotsopoulos, J. L. Duarte, and M. A. M. Hendrix, "Family of multiport bidirectional DC-DC converters," *IEE Proceeding Electric Power Applications*, vol. 153, no. 3, pp. 451–458, May 2006

[5] M. Jafari, Z. Malekjamshidi, G. Lei, T. Wang, G. Platt and J. Zhu, "Design and Implementation of an Amorphous High-Frequency Transformer Coupling Multiple Converters in a Smart Microgrid," *IEEE Trans. Ind. Electron.*, vol. 64, no. 2, pp. 1028-1037, Feb. 2017.

[6] H. Tao, J. L. Duarte, M. A. M. Hendrix, "Three-port triple-half bridge bidirectional converter with zero voltage switching," *IEEE Trans. Power Electron.*, vol. 23, no.2, pp 782–792, March 2008

[7] Junjun Zhang, Hongfei Wu, Xiaoqing Qin and Yan Xing, "PWM Plus Secondary-Side Phase-Shift Controlled Soft-Switching Full-Bridge Three-Port Converter for Renewable Power Systems," *IEEE Trans. Ind. Electron.*, vol. 62, no. 11, pp. 7061-7072, Nov. 2015

[8] C. Zhao, S.D.Round, and J.W.Kolar, "An isolated three-port bidirectional DC–DC converter with decoupled power flow management," *IEEE Trans. Power Electron.*, vol. 23, no. 5, pp. 2443–2453, Sep. 2008

[9] L. F. Costa, G. Buticchi and M. Liserre, "Quad-Active-Bridge DC–DC Converter as Cross-Link for Medium-Voltage Modular Inverters," *IEEE Trans. Ind. App.* vol. 53, no. 2, pp. 1243-1253, March-April 2017.

[10] E. L. Barrios, A. Ursúa, L. Marroyo and P. Sanchis, "Analytical Design Methodology for Litz-Wired High-Frequency Power Transformers," *IEEE Trans. Ind. Electron.*, vol. 62, no. 4, pp. 2103-2113, April 2015

[11] Z. Ouyang, O. C. Thomsen and M. A. E. Andersen, "Optimal Design and Tradeoff Analysis of Planar Transformer in High-Power DC–DC Converters," *IEEE Trans. Ind. Electron.*, vol. 59, no. 7, pp. 2800-2810, July 2012

[12] Y. Du, S. Baek, S. Bhattacharya and A. Q. Huang, "High-voltage high-frequency transformer design for a 7.2kV to 120V/240V 20kVA solid state transformer," *IECON 2010*, Glendale, AZ, 2010, pp. 493-498.

[13] I. Villar, U. Viscarret, I. Etxeberria-Otadui and A. Rufer, "Global Loss Evaluation Methods for Nonsinusoidally Fed Medium-Frequency Power Transformers," *IEEE Trans. Ind. Electron.*, vol. 56, no. 10, pp. 4132-4140, Oct. 2009

[14] H. Hämäläinen, J. Pyrhönen, J. Nerg, and J. Talvitie, "AC resistance factor of litz-wire windings used in low-voltage high-power generators," *IEEE Trans. Ind. Electron.*, vol. 61, no. 2, pp. 693–700, Feb. 2014

[15] C. R. Sullivan, "Computationally efficient winding loss calculation with multiple windings, arbitrary waveforms, and two-dimensional or three-dimensional field geometry," *IEEE Trans. Power Electron.*, vol. 16, no. 1, pp. 142-150, Jan 2001

[16] P.L. Dowell, "Effects of eddy currents in transformer windings," *in Proc. IEE*, Vol.113, pp.1387-1394, Aug. 1966

[17] R. P. Wojda and M. K. Kaizimierczuk, "Winding resistance of litz-wire and multi-strand inductors," *IET Power Electron.*, vol. 5, no. 2, pp. 257–268, Feb. 2012

[18] C. R. Sullivan, “Optimal choice for number of strands in a litz-wire transformer winding,” *IEEE Trans. Power Electron*., vol. 14, no. 2, pp. 283–291,Mar. 1999
[19] J. Lammeraner and M. Stafl, Eddy Currents, 1st ed. London, U.K.: Iliffe
Books, Ltd., 1966, Ch. 7
[20] M. Bartoli, N. Noferi, A. Reatti, and M. K. Kazimierczuk, “Modeling litz wire winding losses in high-frequency power inductors,” in *Proc. IEEE PESC*, 1996, pp. 1690–1696
[21] F. Tourkhani and P. Viarouge, “Accurate analytical model of winding losses in round litz wire windings,” *IEEE Trans. Magn*., vol. 37, no. 1, pp. 538–543, Jan. 2001
[22] A. W. Lotfi and F. C. Lee, “A high frequency model for Litz wire for switch-mode magnetics,” in *proc. Ind. Appl. Society Annual Meeting*, 1993., Toronto, Ont., 1993, pp. 1169-1175, Vol.2
[23] X. Nan and C. R. Sullivan, “An equivalent complex permeability model for litz-wire windings,” *IEEE Trans. Ind. Appl*., vol. 45, no. 2, pp. 854– 860, Mar./Apr. 2009
[24] I. Villar, “Multiphysical characterization of medium-frequency power transformers,” Ph.D. dissertation, Faculté des Sciences et Techniques de l’Ingénieur, École Polytechnique Fédérale Lausanne, Lausanne, Switzerland, 2010
[25] J. A. Ferreira, “Improved analytical modeling of conductive losses in magnetic components,” *IEEE Trans. Power Electron*., vol. 9, no. 1, pp. 127–131, Jan. 1994
[26] D. Murthy-Bellur and M. K. Kazimierczuk, “Harmonic winding loss in buck DC-DC converter for discontinuous conduction mode," *IET Power Electron.*, vol. 3, no. 5, pp. 740-754, September 2010.
[27] D. Murthy-Bellur, N. Kondrath and M. K. Kazimierczuk, “Transformer winding loss caused by skin and proximity effects including harmonics in pulse-width modulated DC-DC flyback converters for the continuous conduction mode,” *IET Power Electron.*, vol. 4, no. 4, pp. 363-373, April 2011
[28] F. Xue, R. Yu and A. Q. Huang, “Loss analysis of a high efficiency GaN and Si device mixed isolated bidirectional DC-DC converter,” in *proc. 2016 IEEE APEC,* Long Beach, CA, 2016, pp. 3677-3683
[29] S. Falcones, R. Ayyanar and X. Mao, “A DC–DC Multiport-Converter-Based Solid-State Transformer Integrating Distributed Generation and Storage,” *IEEE Trans. Power Electron.*, vol. 28, no. 5, pp. 2192-2203, May 2013.
[30] M. Jafari, Z. Malekjamshidi and J. Zhu, “Accurate copper loss analysis of a multi-winding high-frequency transformer for a magnetically-coupled residential micro-grid,” in *Proc. 20th Int. Conf. on Electrical Machines and Systems (ICEMS)*, Sydney, NSW, 2017, pp. 1-6.
[31] J. A. Ferreira, “A Analytical computation of AC resistance of round and rectangular litz wire windings," in *IEE Proc. B-Electric Power Applications*, vol. 139, no. 1, pp. 21-25, Jan. 1992
[32] A. Reatti and M. K. Kazimierczuk, “Comparison of various methods for calculating the AC resistance of inductors,” *IEEE Trans. Magn.*, vol. 38, no. 3, pp. 1512-1518, May 2002
[33] Kaizimierczuk. M. K. “ *High-Frequency Magnetic Components*” (Wiley, Chichester, UK, 2009)
[34] R. Wrobel and P. H. Mellor, “Thermal Design of High-Energy-Density Wound Components,” *IEEE Trans. Ind. Electron*., vol. 58, no. 9, pp. 4096-4104, Sept. 2011.
[35] R. Wrobel, A. Mlot and P. H. Mellor, “Contribution of End-Winding Proximity Losses to Temperature Variation in Electromagnetic Devices,” *IEEE Trans. Ind. Electron*, vol. 59, no. 2, pp. 848-857, Feb. 2012.
[36] J. G. Hayes, D. Cashman, M. G. Egan, T. O'Donnell and N. Wang, “Comparison of Test Methods for Characterization of High-Leakage Two-Winding Transformers,” *IEEE Trans.Ind.App.*, vol. 45, no. 5, pp. 1729-1741, Sept.-oct. 2009.
[37] H. Akagi, T. Yamagishi, N. M. L. Tan, S. i. Kinouchi, Y. Miyazaki and M. Koyama., “Power-Loss Breakdown of a 750-V 100-kW 20-kHz Bidirectional Isolated DC–DC Converter Using SiC-MOSFET/SBD Dual Modules,” *IEEE Trans. Ind. App*, vol. 51, no. 1, pp. 420-428, Jan.-Feb. 2015
[38] A. K. Sadigh, V. Dargahi and K. A. Corzine, “Investigation of Conduction and Switching Power Losses in Modified Stacked Multicell Converters,” *IEEE Trans. Ind. Electron.*, vol. 63, no. 12, pp. 7780-7791, Dec. 2016
[39] G. Feix, S. Dieckerhoff, J. Allmeling and J. Schonberger, “Simple methods to calculate IGBT and diode conduction and switching losses,” in *proc.13th European Conference on Power Electronics and Applications*, Barcelona, 2009, pp. 1-8
[40] Graovac.D, Pürschel.M, “IGBT Power Losses Calculation Using the Data-Sheet Parameters,” Application Note, V 1.1, January 2009

Mohammad Jafari. (M’12) received the B.E. degree from Shiraz University, Shiraz, Iran, in 1998, the M.E. degree from Guilan University, Rasht, Iran, in 2001 and, the Ph.D. degree from University of Technology Sydney (UTS), Sydney, Australia, in 2017 all in electrical engineering.

From 2001 to 2011, he contributed to the design and development of many industrial power electronic projects. Since 2012, he has been with the UTS as a lecturer. His current research interests include power electronic converters and drives, renewable energy systems and smart micro-grids.

Zahra Malekjamshidi (S’13) received the B.E. and M.E. degrees from Shiraz University, Shiraz, Iran, in 1998, and 2001 respectively, both in electrical engineering. She is currently working toward the Ph.D. degree at the University of Technology Sydney (UTS), Sydney, Australia. From 2002 to 2012, she worked as a research engineer and contributed to the design and development power electronic projects. Her current research interests include matrix converters, dc-dc converters, renewable energy technologies and smart micro-grids.

Jianguo Zhu (S’93–M’96–SM’03) received the B.E. degree in 1982 from Jiangsu Institute of Technology, Jiangsu, China, the M.E. degree in 1987 from Shanghai University of Technology, Shanghai, China, and the Ph.D. degree in 1995 from the University of Technology Sydney (UTS), Sydney, Australia, all in electrical engineering. He was appointed a lecturer at UTS in 1994 and promoted to full professor in 2004 and Distinguished Professor of Electrical Engineering in 2017. In 2018, he joined the University of Sydney, Australia, as a full professor and Head of School, School of Electrical and Information Engineering. His research interests include computational electromagnetics, measurement and modelling of magnetic properties of materials, electrical machines and drives, power electronics, renewable energy systems and smart micro grids.